ROYAL SOCIETY OF CHEMISTRY

PAPER

Check for updates

Coordination units of Mn^{2+} modulation toward tunable emission in zero-dimensional bromides for white light-emitting diodes†

Guojun Zhou, ‡*^{a} Jialiang Ding,‡^{a} Xingxing Jiang, ^{b} Jian Zhang, ^{a} Maxim S. Molokeev, ^{cde} Qiqiong Ren,^{a} Jun Zhou, ^{f} Shili Li^a and Xian-Ming Zhang *^{ag}

Organic–inorganic metal halides have become a multifunctional platform for manipulating photoluminescence due to highly efficient and tunable emissions, especially for lead-free Mn^{2+}-based halides. Herein, the zero-dimensional (0D) bromides of $(C_5H_{14}N_3)_2MnBr_4$ and $(CH_6N_3)_2MnBr_4$ with different coordination environments were designed and synthesized by a solvent evaporation method. They exhibit green and red broadband emission peaks at 528 nm and 627 nm with high photoluminescence quantum yields of 86.83% and 61.91%, respectively, which are attributed to the d–d transition ($^4T_1(G) \rightarrow {}^6A_1(S)$) of $[MnBr_4]^{2-}$ tetrahedral and $[Mn_3Br_{12}]^{6-}$ octahedral units. The cases emphasize the effect of organic ligands on the intrinsic emissions of Mn^{2+} ions, thereby revealing the luminescence mechanism of Mn^{2+} ions in 0D isolated structures through the Tanabe–Sugano (TS) energy diagram. Thanks to their bright and stable emissions, the fabricated white light-emitting diode (LED) based on $(C_5H_{14}N_3)_2MnBr_4$ and $(CH_6N_3)_2MnBr_4$ provides an outstanding color rendering index (R_a) of 90.8 at a correlated color temperature (CCT) of 3709 K, along with the CIE chromaticity coordinates of (0.3985, 0.3979) and a luminous efficacy of 51.2 lm W^{-1}. This work aims at clarifying the relationship between the coordination units of Mn^{2+} and tunable emissions, and in particular, proposes a new strategy to explore phosphors excited by blue light for white LEDs.

^{a} *Key Laboratory of Magnetic Molecules and Magnetic Information Materials (Ministry of Education), School of Chemistry and Material Science, Shanxi Normal University, Taiyuan 030006, China. E-mail: zhougj@sxnu.edu.cn, zhangxm@dns.sxnu.edu.cn; Tel: +86-0357-2051402*

^{b} *China Technical Institute of Physics and Chemistry, Chinese Academy of Sciences, Beijing 100190, China*

^{c} *Laboratory of Crystal Physics, Kirensky Institute of Physics, Federal Research Center KSC SB RAS, Krasnoyarsk 660036, Russia*

^{d} *Department of Engineering Physics and Radioelectronics, Siberian Federal University, Krasnoyarsk 660041, Russia*

^{e} *Research and Development Department, Kemerovo State University, Kemerovo, 650000, Russia*

^{f} *Department of Physics, Beijng Technology and Business University, Beijing 100048, China*

^{g} *College of Chemistry & Chemical Engineering, Key Laboratory of Interface Science and Engineering in Advanced Material, Ministry of Education, Taiyuan University of Technology, Taiyuan, Shanxi 030024, P. R. China*

† Electronic supplementary information (ESI) available: Fig. S1–S5 showing PXRD patterns, FTIR spectra, UV-visible absorption spectra, thermogravimetric (TG) curves, and temperature-dependent PL spectra of $(C_5H_{14}N_3)_2MnBr_4$ and $(CH_6N_3)_2MnBr_4$; Table S1 listing fractional atomic coordinates and isotropic or equivalent isotropic displacement parameters. Table S2 listing the main bond lengths. Table S3 listing hydrogen-bond geometry in the structures. Crystallographic data of $(C_5H_{14}N_3)_2MnBr_4$ and $(CH_6N_3)_2MnBr_4$ (CIF). CCDC 2094640 and 2094641. For ESI and crystallographic data in CIF or other electronic format see DOI: 10.1039/d1tc05680h

‡ These authors contributed equally.

1. Introduction

Organic–inorganic metal halides (OIMHs) formed by self-assembly of organic cations and inorganic anions have received extensive interest in many fields, such as light-emitting diodes (LEDs), photodetectors, ferroelectrics, solar cells, and so on.[1–6] Compared to all-inorganic metal halides, OIMHs have a high degree of design flexibility owing to the various structural dimensions and abundant chemical components.[7–9] Among them, as a kind of hybrid material composed of organic cations and spatially isolated anions, zero-dimensional (0D) OIMHs provide an excellent platform for the development of high-efficiency emitting materials;[10–12] in particular, 0D Mn^{2+}-based OIMHs have attracted much attention.[13–16]

Although most of the reported OIMHs possess excellent luminescence properties, the toxicity of Pb^{2+} and instability limit their practical applications, which lead to the development of lead-free OIMHs becoming imminent.[17–20] In comparison, the Mn^{2+}-based OIMHs present the advantages of environmental friendliness, good stability and tunable emission. As is well known the transition metal ion Mn^{2+} has a 3d^5 electronic configuration and generally exhibits visible (vis) photoluminescence (PL) originating from the $^4T_1 \rightarrow {}^6A_1$ transition, which

This journal is © The Royal Society of Chemistry 2022

J. Mater. Chem. C, 2022, **10**, 2095–2102 | **2095**

strongly depends on the crystal field surroundings of Mn^{2+} in the host lattice.[21,22] Octahedrally coordinated Mn^{2+} shows an orange to red emission with a large full width at half maximum (FWHM > 60 nm), while tetrahedrally coordinated Mn^{2+} exhibits a green–yellow emission (500–550 nm) with a small FWHM of 25–60 nm.[23–27] So far, Mn^{2+}-doped metal halides with orange–red emissions have been reported the most,[28–34] but unfortunately, they cannot be well applied in the field of solid-state lighting due to the shortcoming that almost all of them cannot be excited by blue light, resulting in a low efficiency for white LED devices. Most of the Mn^{2+}-based OIMHs exhibit a narrow-band green emission.[13–15,35–39] Even if these 0D analogues show a high-efficiency Mn^{2+} emission with near-unity photoluminescence quantum yields (PLQYs), the relatively small FWHM (20–60 nm) of the PL peak makes it impossible to endow high-performance white LED devices with a high color rendering index (R_a) for the application of solid-state lighting.[40,41] In addition, the 0D Mn^{2+}-based OIMHs with a highly efficient red emission have also been reported and popularized recently. However, only a small amount of 0D Mn^{2+}-based OIMHs that can emit red light was investigated so far,[3,24,42,43] and there is no comparative analysis of their luminescence mechanism by binding to that of 0D Mn^{2+}-based OIMHs with green light emission.

Organic ligands, as a key component to modify Mn2+ coordination units in OIMHs, play an irreplaceable role in the construction of their electronic band structures and crystal structures. In this work, we employed organic cations including guanidine hydrobromide and 1,1,3,3-tetramethylguanidine hydrobromide, and synthesized two kinds of 0D Mn2+-based bromides with broadband emission by reacting them with $MnBr^2$ respectively. Efficient room-temperature phosphorescence originating from the d−d transition ($^4T_1$–$^6A_1$) of Mn^{2+} is demonstrated in these compounds and shows a strong dependence on the crystal field surroundings of Mn^{2+}. Furthermore, we elaborated the electronic features and optical absorption according to the Tanabe–Sugano (TS) diagram of the $3d^5$ electron orbital of Mn^{2+} and extended the principle by employing organic ligands to tune the Mn^{2+} emission in 0D bromides. The as-fabricated white LED device with a high R_a of 90.8 at a correlated color temperature (CCT) of 3709 K demonstrates that $(C_5H_{14}N_3)_2MnBr_4$ and $(CH_6N_3)_2MnBr_4$ can be promising as rare-earth-free and lead-free phosphors in the field of solid-state lighting. Our realizable cases provide a deep understanding about the coordination units of Mn^{2+} toward tunable emission and propose a new way to explore high-performance OIMHs pumped by blue light for white LEDs.

2. Experimental section

2.1 Materials and preparation

Guanidine hydrobromide (CH_6N_3Br, 98%, Sigma-Aldrich), 1,1,3,3-tetramethylguanidine ($C_5H_{13}N_3$, 98%, Energy chemical), manganese bromide tetrahydrate ($MnBr_2·4H_2O$, 98%, Aladdin), hydrobromic acid (HBr, 40%, Aladdin), acetonitrile (CH_3CN, 99.5%, Kermel) and ethanol (C_2H_5OH, 99.7%, Guangfu) were all used as received.

The single crystals of $(C_5H_{14}N_3)_2MnBr_4$ and $(CH_6N_3)_2MnBr_4$ were synthesized by a solvent volatilization method. For $(C_5H_{14}N_3)_2MnBr_4$, 1.1518 g (10 mmol) of $C_5H_{13}N_3$ were dissolved in 3 mL of ethanol, then 2 mL of hydrobromic acid (40%) were dropped slowly into it. Again, 1.434 g (5 mmol) of $MnBr_2·4H_2O$ were added into the solution, followed by placing the solution on the magnetic stirrer and stirring it until a clear solution was formed; then the solution was slowly evaporated at room temperature and the single crystals could be obtained after about one week. The obtained crystals were washed repeatedly three times with C_2H_5OH, and then filtered with a Büchner funnel. Finally, the crystals were dried at 50 °C in an oven for 24 hours. For $(CH_6N_3)_2MnBr_4$, 0.70 g (5 mmol) of CH_6N_3Br and 0.717 g (2.5 mmol) of $MnBr_2·4H_2O$ were thoroughly dissolved in 5 mL of acetonitrile. The solution was then slowly evaporated at room temperature and the single crystals of $(CH_6N_3)_2MnBr_4$ can be obtained after about one week. The obtained crystals were washed repeatedly three times with CH_3CN, and then filtered by using the Büchner funnel. Finally, the crystals were dried at 50 °C in an oven for 24 hours.

2.2 Characterization

The single-crystal X-ray diffraction data of $(C_5H_{14}N_3)_2MnBr_4$ and $(CH_6N_3)_2MnBr_4$ were collected at room temperature using the XtaLAB AFC12 X-ray four-circle single crystal diffractometer (Rigaku) equipped with a CCD-detector, a graphite monochromator and a Mo Kα radiation source. The powder X-ray diffraction data of $(CH_6N_3)_2MnBr_4$ and $(C_5H_{14}N_3)_2MnBr_4$ were collected at room temperature with an X-ray diffractometer (Cu-Kα radiation). The photoluminescence (PL) spectra, photoluminescence excitation (PLEX) spectra, photoluminescence emission (PLEM) spectra, fluorescence decay curve and PLQYs were measured using a FLS-920 fluorescence spectrometer (Edinburgh Instruments Ltd. UK). Temperature-dependent emission spectra were measured on the same spectrophotometer installed with a heating apparatus as the heating source. Thermogravimetric analysis (TGA) was performed on a SETARAM 131 LABSYS device under an argon stream at a heating rate of 10 °C min^{-1} from RT to 800 °C. The emission spectra, correlated color temperature (CCT), luminous efficacy, and CIE coordinates of the LED devices were measured using an integrating sphere spectroradiometer system (ATA-100, Everfine).

2.3 Computational methods

The electronic band structure and density of states (DOS) were calculated by CASTEP based on plane-wave pseudopotential density functional theory (DFT).[44] Perdew–Burke–Ernzerhof (PBE) functionals in the generalized gradient approximation (GGA) form were used for electronic structure calculations.[45] The optimized norm-conserving pseudopotential in Kleinman–Bylander allows us to use a small plane basis set without compromising the required accuracy of the calculation. A kinetic energy cut off value of 900 eV and a Monkhorst–Pack k-point mesh spanning less than 0.03 Å^{-1} in the Brillouin zone were chosen. The Broyden–Fletcher–Goldfarb–Shanno (BFGS) minimization scheme was employed and the convergence criteria for the structure optimization were set to $5.0 × 10^{-5}$ eV

2096 | *J. Mater. Chem. C*, 2022, **10**, 2095–2102

This journal is © The Royal Society of Chemistry 2022

per atom, 0.1 eV per Å, 0.2 GPa and 5.0×10^{-3} GPa which is energy, maximum force, maximum stress and maximum displacement, respectively.

3. Results and discussion

3.1 Synthesis and structure evolution

The Mn^{2+}-based bromides of $(C_5H_{14}N_3)_2MnBr_4$ and $(CH_6N_3)_2MnBr_4$ were synthesized by a solvent volatilization method, and their single crystal data are collected at room temperature (RT). The orientation matrix and cell parameters of $(C_5H_{14}N_3)_2MnBr_4$ and $(CH_6N_3)_2MnBr_4$ were defined and refined for the set of 5077 and 23264 reflections, respectively. The unit cell corresponds to a monoclinic symmetry in both cases. Space groups $C2/c$ and $P2_1/c$ were determined by utilizing the statistical analysis of the intensities of all the reflections. The absorption correction using spherical harmonics was applied using the ABSPAK program. The crystal structure was solved by using package SHELXS and refined *via* the anisotropic approach for non-hydrogen atoms using the SHELXL program.[46] All the hydrogen atoms of the ligands were positioned geometrically as riding on their parent atoms with $d(C–H) = 0.97$ Å for the C–H bonds and $d(N–H) = 0.86$ Å for all other N–H bonds and $U_{iso}(H) = 1.2U_{eq}$ (C, N). The main crystal data are shown in Table 1. The crystallographic data are deposited in the Cambridge Crystallographic Data Centre (CCDC # 2094640–2094641). The coordinates of atoms are in Table S1 (ESI†), and the main bond lengths are shown in Table S2 (ESI†). The asymmetric part of the $(C_5H_{14}N_3)_2MnBr_4$ unit cell includes one organic cation of $[C_5H_{14}N_3]^{2+}$, one half of Mn^{2+} and two Br^- ions. The Mn^{2+} ion is coordinated with four Br^- ions to form the $[MnBr_4]^{2-}$ tetrahedron (Fig. 1a). The tetrahedra are isolated from each other to form a 0D structure (Fig. 1b). There are two N–H···Br hydrogen bonds (Table S3, ESI†), which join the organic cations $[C_5H_{14}N_3]^{2+}$ with $[MnBr_4]^{2-}$ tetrahedra and form a three-dimensional (3D) net. The asymmetric part of the $(CH_6N_3)_2MnBr_4$ unit cell contains six organic cations of $[CH_6N_3]^{2+}$, three Mn^{2+} and twelve Br^- ions. All Mn^{2+} ions are coordinated by six Br^- ions to form $MnBr_6$ octahedra (Fig. 1d). These octahedra are linked with each other by sharing faces to form an isolated 0D block (Fig. 1c). There are 33
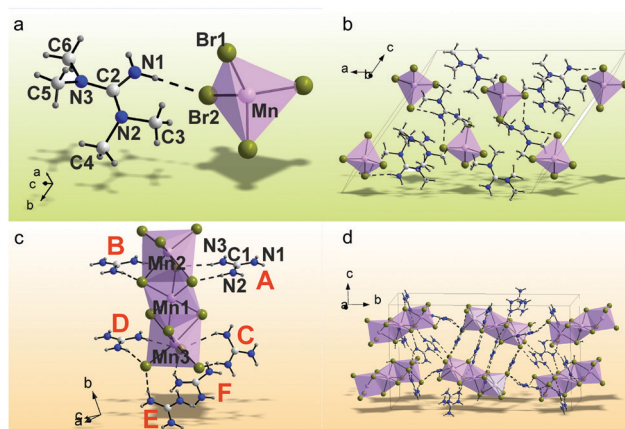

Fig. 1 Crystal asymmetric structure units of $(C_5H_{14}N_3)_2MnBr_4$ (a) and $(CH_6N_3)_2MnBr_4$ (c). The atoms in the asymmetric part of the unit cell $(C_5H_{14}N_3)_2MnBr_4$ (b) and $(CH_6N_3)_2MnBr_4$ (d) are labeled, the hydrogen bonds in which are presented as dashed lines. The independent $[CH_6N_3]^+$ cations in the Figure (c) are marked by bold labels A–E.

N–H···Br hydrogen bonds (Table S3, ESI†) between the organic cations $[CH_6N_3]^{2+}$ and $[Mn_3Br_{12}]^{6-}$ polyhedra, all of which stack together to form a 3D net. Fig. S1 (ESI†) shows the PXRD patterns of $(C_5H_{14}N_3)_2MnBr_4$ and $(CH_6N_3)_2MnBr_4$, indicating that the obtained powders are pure phases and are consistent with their single crystal phases, respectively. In addition, the organic functional groups were characterized by FTIR spectra in Fig. S2 (ESI†).[47,48] It is observed that $(C_5H_{14}N_3)_2MnBr_4$ and $(CH_6N_3)_2MnBr_4$ both exhibit the absorption peaks at $\sim$3300 cm^{-1}, $\sim$1650 cm^{-1} and $\sim$1000 cm^{-1}, which are ascribed to the stretching vibration, blending vibration of N–H and the C–N stretching vibration, respectively. Compared with $(CH_6N_3)_2MnBr_4$, $(C_5H_{14}N_3)_2MnBr_4$ possess additional absorption peaks at $\sim$2950 cm^{-1}, $\sim$2850^{-1} and $\sim$1370 cm^{-1}, which are assigned to the –CH$_3$ asymmetric, symmetric stretching vibrations and deformation vibrations, respectively.

3.2 Photoluminescence tuning and mechanism

The transition metal ion Mn^{2+} has a 3d^5 electronic configuration. Since the 3d orbital electrons of Mn^{2+} are exposed in the outer layer, the wavelength position of the emission band of Mn^{2+} is strongly affected by the crystal field environment. In view of this, the coordination units of Mn^{2+} can be modified by employing different organic ligands toward tunable emission in 0D bromides. The photoluminescence (PL) and photoluminescence excitation (PLE) spectra of $(C_5H_{14}N_3)_2MnBr_4$ and $(CH_6N_3)_2MnBr_4$ are shown in Fig. 2a and b. They exhibit a green emission at 528 nm and a red emission at 627 nm under excitation at 365 and 375 nm, respectively, which are originated from the d–d transition ($^4T_1(G) \rightarrow {}^6A_1(S)$) of four coordinated $[MnBr_4]^{2-}$ units and six coordinated $[Mn_3Br_{12}]^{6-}$ units, respectively. In particular, $(C_5H_{14}N_3)_2MnBr_4$ and $(CH_6N_3)_2MnBr_4$ presents absorption peaks at the blue region, corresponding to the transitions of $^6A_1 \rightarrow {}^4A_1(G)$, $^4E(G)$ and $^6A_1 \rightarrow {}^4T_2(G)$, which enables them to be applied to white LEDs pumped by blue light. The UV-visible absorption spectra of $(C_5H_{14}N_3)_2MnBr_4$ and

Table 1 Main crystal structure parameters of $(C_5H_{14}N_3)_2MnBr_4$ and $(CH_6N_3)_2MnBr_4$

Chemical formula	$(C_5H_{14}N_3)_2MnBr_4$	$(CH_6N_3)_2MnBr_4$
Weight, g mol^{-1}	606.96	494.76
Temperature (K)	293	293
Space group, Z	$C2/c$, 4	$P2_1/c$, 12
a (Å)	19.215 (3)	9.0171 (3)
b (Å)	9.2604 (7)	27.9628 (10)
c (Å)	15.366 (2)	16.1020 (5)
β (°)	125.51 (2)	93.016 (3)
V (Å^3)	2225.6 (6)	4054.4 (2)
ρ_{calc}, g cm^{-3}	1.811	2.432
R_{int}	0.0496	0.0546
$2\theta_{max}$, °	58.34	59.18
$R1$ $[F_o > 4\sigma(F_o)]$	0.0697	0.0508
$wR2$	0.1913	0.1363
Goof	0.828	0.898

This journal is © The Royal Society of Chemistry 2022

J. Mater. Chem. C, 2022, **10**, 2095–2102 | **2097**

Fig. 2 The photoluminescence (PL) and photoluminescence excitation (PLE) spectra of $(C_5H_{14}N_3)_2MnBr_4$ (a) and $(CH_6N_3)_2MnBr_4$ (b) at room temperature (RT). Photoluminescence decay curves of $(C_5H_{14}N_3)_2MnBr_4$ (c) and $(CH_6N_3)_2MnBr_4$ (d) at RT under excitation at 365 nm, emission at 528/627 nm.

$(CH_6N_3)_2MnBr_4$ are shown in Fig. S3 (ESI†). The decay curves monitored at λ_{em} = 528 nm and λ_{em} = 627 nm were collected under 365 nm excitation, as shown in Fig. 2c and d. They can be fitted by utilizing the following decay equation:[49,50]

$$I(t) = I_0 + A \exp(-t/\tau) \tag{1}$$

where $I(t)$ and I_0 are the luminescence intensity at time t and $t \gg \tau$, respectively. A is a constant, and τ is the decay time, which is an exponential component. The lifetimes of $(C_5H_{14}N_3)_2MnBr_4$ and $(CH_6N_3)_2MnBr_4$ are determined to be 0.31 and 1.04 ms, respectively, which possess relatively short lifetimes. Among them, the lifetime value of $(C_5H_{14}N_3)_2MnBr_4$ is consistent with that reported in the literature,[14,15] which indicates that the green-light emission originates from the d–d transition ($^4T_1(G) \rightarrow {}^6A_1(S)$) of four coordinated $[MnBr_4]^{2-}$ units. The lifetime value of $(CH_6N_3)_2MnBr_4$ has not been proven, but compared with the similar A_2BX_4 type Mn^{2+}-based chlorides,[42,43] its lifetime value is smaller, which is in line with the law of the influence of halogen ions on the lifetime in green-emitting Mn^{2+}-based halides.[15] Accordingly, the red emission peaked at 627 nm is attributed to the d–d transition ($^4T_1(G) \rightarrow {}^6A_1(S)$) of six coordinated $[Mn_3Br_{12}]^{6-}$ units.

In addition, $(C_5H_{14}N_3)_2MnBr_4$ and $(CH_6N_3)_2MnBr_4$ both exhibit the broadband emissions, with a relatively large FWHM of 58 nm and 79 nm at RT, respectively, which is conducive to the application of such materials in solid-state lighting. Fig. 3a and b show the temperature-dependent PL spectra in the range of 80–300 K. The emission peak position of $(C_5H_{14}N_3)_2MnBr_4$ hardly changed, while the emission peak position of $(CH_6N_3)_2MnBr_4$ showed a blue-shift from 655 nm to 627 nm, which is mainly ascribed to the following two reasons. On the

one hand, $(CH_6N_3)_2MnBr_4$ has a high crystal field strength, and the thermally induced host lattice expansion has a significant effect on the crystal field strength, resulting in the value of that reduce significantly.

On the other hand, the crystal expansion reduced the spin–spin coupling energy (E_{sc}) of locally adjacent Mn^{2+} ions in the crystal such as Frenkel exciton coupling in molecular aggregates.
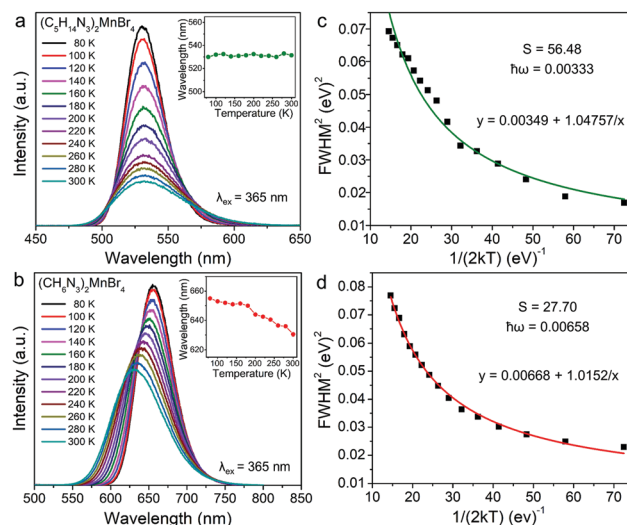

Fig. 3 Temperature-dependent PL spectra of $(C_5H_{14}N_3)_2MnBr_4$ (a) and $(CH_6N_3)_2MnBr_4$ (b) under 365 nm excitation in the range from 80 to 300 K. Inset: the temperature-dependent emission peak. The FWHM fitting curve of $(C_5H_{14}N_3)_2MnBr_4$ (c) and $(CH_6N_3)_2MnBr_4$ (d) as a function of temperature via the eqn (4) to obtain the Huang–Phys factor S and maximum phonon energy $\hbar\omega$.

2098 | *J. Mater. Chem. C*, 2022, **10**, 2095–2102

This journal is © The Royal Society of Chemistry 2022

If the separation between Mn ions increases during the process of crystal expansion, the value of E_{sc} value would decrease clearly. With the increase of temperature, the emission peak of $(CH_6N_3)_2MnBr_4$ shows a blue-shift. In addition, the degree of electron–phonon coupling is defined by the Huang–Rhys factor S,[37,51,52] which can be solved by the following equation:

$$FWHM = 2.36\hbar\omega\sqrt{S\coth\left(\frac{\hbar\omega}{2kT}\right)} \qquad (2)$$

where ω is the phonon frequency, $\hbar\omega$ is the maximum phonon energy, k is the Boltzmann constant, S is Huang–Rhys factor, and $\coth(x) = \frac{e^x + e^{-x}}{e^x - e^{-x}} = 1 + \frac{2}{e^{2x} - 1}$. When $\frac{\hbar\omega}{kT}$ is small enough, $e^{\frac{\hbar\omega}{kT}} - 1 \approx \frac{\hbar\omega}{kT}$, the following equation can be obtained:

$$FWHM^2 = 5.57(\hbar\omega)^2 S\left(1 + \frac{2}{e^{\frac{\hbar\omega}{kT}} - 1}\right)$$

$$= 5.57(\hbar\omega)^2 S\left(1 + \frac{1}{\frac{\hbar\omega}{2kT}}\right) \qquad (3)$$

This can be further written as follows:

$$FWHM^2 = a + \frac{b}{\frac{1}{2kT}} \qquad (4)$$

where $a = 5.57 \times S \times (\hbar\omega)^2$ and $b = 5.57 \times S \times (\hbar\omega)$. The Huang–Rhys factor S reflects the degree of electron–phonon coupling. According to the temperature-dependent PL spectra from 80 to 300 K, the value of $\frac{1}{2kT}$ and $FWHM^2$ can be calculated. Taking $\frac{1}{2kT}$ as the horizontal coordinate and $FWHM^2$ as vertical coordinate, the Huang–Rhys factors S and $\hbar\omega$ of $(C_5H_{14}N_3)_2MnBr_4$ and $(CH_6N_3)_2MnBr_4$ are obtained by fitting, corresponding to $S = 56.48$, $\hbar\omega = 0.00333$ eV and $S = 27.70$, $\hbar\omega = 0.00658$ eV, and the relatively large Huang–Rhys factor S indicates a stronger electron–phonon coupling interaction.

As is well-known, the energy levels of Mn^{2+} ions have different spin multiplicities, and there is a strong interaction with the crystal field and lattice vibration due to the spatial extension of the d electron wave function, especially under the influence of the two factors including the strength of the crystal field (Δ) and covalency (B) of the Mn–ligand bond. To illustrate the energy level distribution of Mn^{2+} ions ($3d^5$), a Tanabe–Sugano (TS) diagram is described in Fig. 4a.[21,22,53] The electrostatic field generated by the ligand splits the original five degenerate d orbitals of Mn^{2+} into two or more groups with different energy levels. The ground state electrons transit to different excited states under light irradiation, and then return to the lowest excited state energy level $^4T_1$ through non-radiative relaxation, and finally the electrons return to the ground state with the production of photons. According to
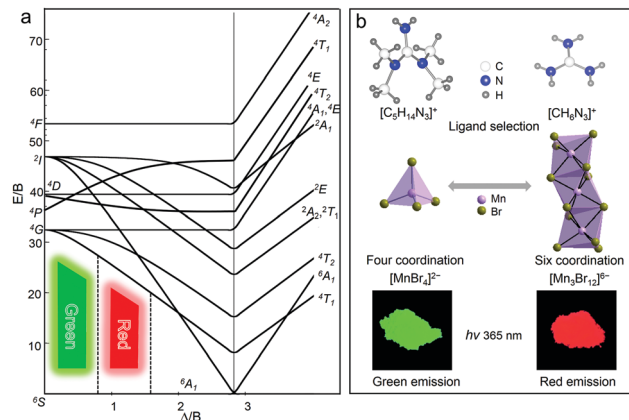

Fig. 4 (a) Tanabe–Sugano (TS) energy diagram of $3d^5$ electron orbital of Mn^{2+}. (b) Modifying the coordination units of Mn^{2+} by selecting different organic ligands to modulate the photoluminescence properties.

the general theory of d-ion emission, the position of the emission peak of Mn^{2+} can be determined by the crystal field strength.[21] In a weaker crystal field, the separation of the $^4T_1$ and $^6A_1$ energy levels is stronger, and hence the green light emission with higher energies is achieved. In contrast, with the increase of the crystal field strength, the emission peak shifts to a lower energy region accompanied by red light emission.

Specifically, the crystal field strength is also affected by the polyhedral distortion index (D) of the polyhedron. With the increase of polyhedral distortion index, the crystal field strength increases, resulting in a large crystal field splitting of the Mn^{2+} 3d level.[54–56] It makes the lowest excited state level $^4T_1$ of Mn^{2+} closer to the ground state and ultimately results in the red-shift of the emission peak of Mn^{2+}. When the manganese halide anions are changed from the tetrahedron to the octahedron, the polyhedral distortion index will change greatly, which can be
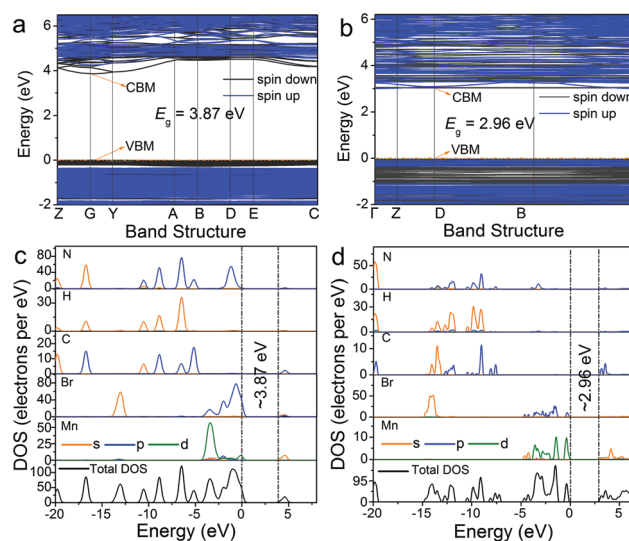

Fig. 5 Electronic energy band structures of $(C_5H_{14}N_3)_2MnBr_4$ (a) and $(CH_6N_3)_2MnBr_4$ (b). The total and orbital projection of partial density of states of $(C_5H_{14}N_3)_2MnBr_4$ (c) and $(CH_6N_3)_2MnBr_4$ (d).

This journal is © The Royal Society of Chemistry 2022

J. Mater. Chem. C, 2022, 10, 2095–2102 | 2099
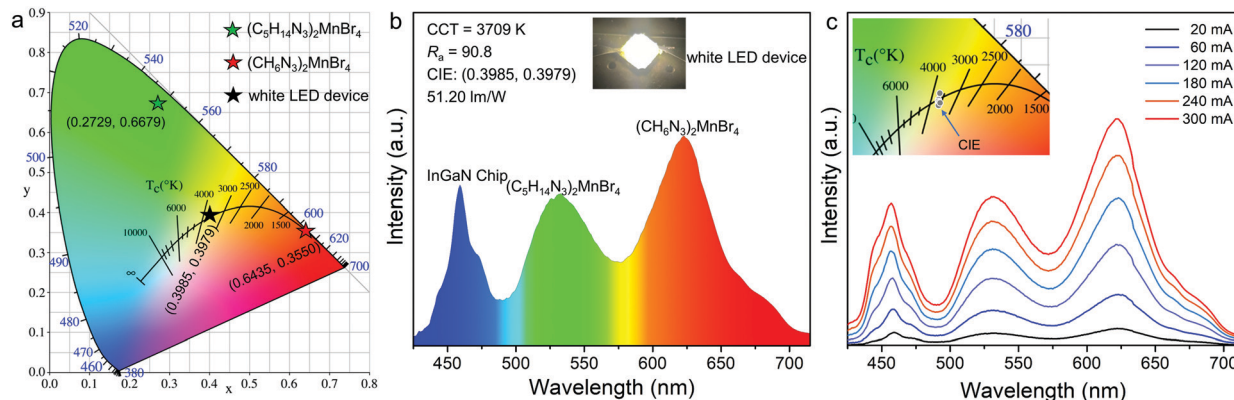
Fig. 6 (a) CIE chromaticity diagram of $(C_5H_{14}N_3)_2MnBr_4$, $(CH_6N_3)_2MnBr_4$, and the fabricated white LED device. (b) Emission spectrum and photograph of the white LED device fabricated with the green emitting $(C_5H_{14}N_3)_2MnBr_4$ and the red emitting $(CH_6N_3)_2MnBr_4$ on a blue LED chip (460 nm) under a current of 20 mA. (c) Emission spectra of the white LED device under the driving currents ranges from 20 to 300 mA, and the inset showing the CIE chromaticity coordinates changes.

defined as[57,58]

$$D = \frac{1}{n}\sum_{i=1}^{n}\frac{|l_i - l_{av}|}{l_{av}} \tag{5}$$

where l_i is the distance between the central atom Mn and the coordinated halogen atom, and l_{av} is the average bond length. For $(C_5H_{14}N_3)_2MnBr_4$, the distortion index of $[MnBr_4]^{2-}$ is 2.16×10^{-3}, while for $(CH_6N_3)_2MnBr_4$, the distortion index of three $MnBr_6$ octahedrons in $[Mn_3Br_{12}]^{6-}$ are 7.97×10^{-3}, 3.55×10^{-2} and 3.73×10^{-2} respectively, with an average value of 2.69×10^{-2}. So the distortion index of $[Mn_3Br_{12}]^{6-}$ is much higher that of $[MnBr_4]^{2-}$. Therefore, compared with $(C_5H_{14}N_3)_2MnBr_4$, the emission peak of $(CH_6N_3)_2MnBr_4$ have a large redshift, which is coincident with the observed experimental phenomenon. As for the MnX_6 units, they usually show orange emission due to the large polyhedral distortion. If these octahedrons combine together by sharing planes with each other, the orange emission shifts to the red emission, which means the increase in distortion index and crystal field strength. As shown in Fig. 4b, the coordination units of Mn^{2+} can be modified by employing different organic cations toward tunable emission in 0D bromides. The Mn^{2+} in $(C_5H_{14}N_3)_2MnBr_4$ is located in the tetrahedral weak field, so it exhibits a green light emission. While the Mn^{2+} in $(CH_6N_3)_2MnBr_4$ is located in the octahedral strong field and these $MnBr_6$ octahedral units form a trimetric $[Mn_3Br_{12}]^{6-}$ unit by sharing planes with each other, so it exhibits a red light emission.

In addition, the electronic energy band structures of 0D bromides with different coordination units of Mn^{2+} are calculated based on the density functional theory (DFT) approach. As illustrated in Fig. 5a and b, the calculated energy gaps for $(C_5H_{14}N_3)_2MnBr_4$ and $(CH_6N_3)_2MnBr_4$ are estimated to be around 3.87 eV at the G point of the Brillouin zone and 2.96 eV at the D point of the Brillouin zone, respectively. The total density states (TDOS) and orbital-projected partial density of states (PDOS) diagrams for $(C_5H_{14}N_3)_2MnBr_4$ and $(CH_6N_3)_2MnBr_4$ (Fig. 5c and d) indicate that the electronic states in the valence band maximum (VBM) are mainly attributed to Br-p and Mn-d orbitals, while those in

the conduction band minimum (CBM) are said to principally originate from organic groups.

3.3 Stability and application for LEDs

The 0D bromides of $(C_5H_{14}N_3)_2MnBr_4$ and $(CH_6N_3)_2MnBr_4$ can be effectively excited by a 450 nm blue light and exhibit relatively high photoluminescence quantum yields (PLQYs) of 86.83% and 61.91%, which enables the corresponding white light LED devices encapsulated by them to achieve a high luminous efficacy in the practical application of solid-state lighting. Meanwhile, their chemical stabilities and temperature quenching (TQ) behaviors were evaluated. The thermogravimetric (TG) results (Fig. S4, ESI†) show that $(C_5H_{14}N_3)_2MnBr_4$ and $(CH_6N_3)_2MnBr_4$ are chemically stable up to 281 °C and 289 °C, respectively. The temperature dependent PL spectra (Fig. S5, ESI†) indicate that their thermal quenching behaviors are obvious, especially after reaching 100 °C. To further evaluate their practical application prospects in solid-state lighting, the white LED device was fabricated by utilizing the green-emitting $(C_5H_{14}N_3)_2MnBr_4$ and red-emitting $(CH_6N_3)_2$-$MnBr_4$ (Fig. 6a and b). The results present a correlated color temperature of 3709 K, along with CIE chromaticity coordinates of (0.3985, 0.3979), which means that there is no need to add commercial phosphors containing rare earth as a strategic resource to produce white light emission. The white LED device exhibits a luminous efficacy (LE) of 51.20 lm W^{-1} and a high color rendering index (R_a) of 90.8, indicating the potential of the as-synthesized Mn^{2+}-based 0D bromides in solid-state lighting. Moreover, the emission spectra and enlarged view of CIE chromaticity coordinates present no remarkable change under different driving currents from 20 to 300 mA (Fig. 6c), revealing a good electroluminescence stability of the fabricated white LEDs. It is found that the 0D bromides of $(C_5H_{14}N_3)_2MnBr_4$ and $(CH_6N_3)_2MnBr_4$ are suitable to act as the high-performance green and red phosphors for white LED applications.

4. Conclusions

In summary, the 0D bromides of $(C_5H_{14}N_3)_2MnBr_4$ and $(CH_6N_3)_2MnBr_4$ with variable coordination units of Mn^{2+} were

2100 | *J. Mater. Chem. C*, 2022, **10**, 2095–2102

This journal is © The Royal Society of Chemistry 2022

designed and synthesized by a facile method of solvent evaporation. They exhibit a green emission at 528 nm and a red emission at 627 nm with a relatively large FWHM of 59 nm and 79 nm under excitation under UV/blue light, which are attributed to the d–d transition ($^4T_1(G) \rightarrow {}^6A_1(S)$) of four coordinated $[MnBr_4]^{2-}$ units and six coordinated $[Mn_3Br_{12}]^{6-}$ units, respectively. According to the temperature-dependent PL spectra from 80 K to 300 K and Tanabe–Sugano (TS) energy diagram, the 0D bromides of $(C_5H_{14}N_3)_2MnBr_4$ and $(CH_6N_3)_2MnBr_4$ show relatively large Huang–Rhys factor S ($S = 56.48$; $S = 27.70$), and the distortion index of $[Mn_3Br_{12}]^{6-}$ ($D = 2.69 \times 10^{-2}$) is much higher than that of $[MnBr_4]^{2-}$ ($D = 2.16 \times 10^{-3}$), resulting in the emission position of $(CH_6N_3)_2MnBr_4$ having a large redshift compared to that of $(C_5H_{14}N_3)_2MnBr_4$. The cases emphasize the influence of organic ligands on the intrinsic emissions of Mn^{2+} ions, and it is found that the 0D bromides of $(C_5H_{14}N_3)_2MnBr_4$ and $(CH_6N_3)_2MnBr_4$ are suitable to act as the high-performance green and red phosphors for white LED applications. The fabricated white LED device shows an excellent R_a of 90.8 at a correlated color temperature of 3709 K, along with CIE chromaticity coordinates of (0.3985, 0.3979). This work aims at clarifying the relationship between the coordination units of Mn^{2+} and emission tuning, and in particular proposes a new way to explore phosphors excited by blue light for white LEDs.

Author contributions

G. Z. and M. X. Z. conceived the project, wrote and revised the paper, and was primarily responsible for the experiment. J. D. synthesized the materials, performed the experimental characterization, and wrote a part of the paper. X. J. and J. Z. performed the DFT calculations. M. M performed the structure analysis. Q. R., J. Z., and S. L. contributed the luminescence mechanism analysis. All authors contributed to the general discussion.

Conflicts of interest

There are no conflicts to declare.

Acknowledgements

Notes and references

1 L. N. Quan, B. P. Rand, R. H. Friend, S. G. Mhaisalkar, T. W. Lee and E. H. Sargent, *Chem. Rev.*, 2019, **119**, 7444–7477.

2 Y. H. Dong, Y. S. Zou, J. Z. Song, X. F. Song and H. B. Zeng, *J. Mater. Chem. C*, 2017, **5**, 11369–11394.

3 Y. Zhang, W. Q. Liao, D. W. Fu, H. Y. Ye, Z. N. Chen and R. G. Xiong, *J. Am. Chem. Soc.*, 2015, **137**, 4928–4931.

4 J. Y. Kim, J.-W. Lee, H. S. Jung, H. Shin and N.-G. Park, *Chem. Rev.*, 2020, **120**, 7867–7918.

5 Q. Q. He, C. K. Zhou, L. J. Xu, S. Lee, X. S. Lin, J. Neu, M. Worku, M. Chaaban and B. W. Ma, *ACS Mater. Lett.*, 2020, **2**, 633–638.

6 P. P. Du, L. Gao and J. Tang, *Front. Optoelectron.*, 2020, **13**, 235–245.

7 G. J. Zhou, B. B. Su, J. L. Huang, Q. Y. Zhang and Z. G. Xia, *Mater. Sci. Eng., R*, 2020, **141**, 100548.

8 P. F. Fu, S. L. Hu, J. Tang and Z. W. Xiao, *Front. Optoelectron.*, 2021, **14**, 252–259.

9 C. K. Zhou, H. Lin, S. Lee, M. Chaaban and B. W. Ma, *Mater. Res. Lett.*, 2018, **6**, 552–569.

10 L. J. Xu, S. Lee, X. Lin, L. Ledbetter, M. Worku, H. Lin, C. K. Zhou, H. Liu, A. Plaviak and B. W. Ma, *Angew. Chem., Int. Ed.*, 2020, **59**, 14120–14123.

11 M. Z. Li and Z. G. Xia, *Chem. Soc. Rev.*, 2021, **50**, 2626–2662.

12 C. K. Zhou, L. J. Xu, S. Lee, H. R. Lin and B. W. Ma, *Adv. Opt. Mater.*, 2020, **9**, 2001766.

13 L. L. Mao, P. J. Guo, S. X. Wang, A. K. Cheetham and R. Seshadri, *J. Am. Chem. Soc.*, 2020, **142**, 13582–13589.

14 G. J. Zhou, Z. Y. Liu, J. L. Huang, M. S. Molokeev, Z. W. Xiao, C. G. Ma and Z. G. Xia, *J. Phys. Chem. Lett.*, 2020, **11**, 5956–5962.

15 V. Morad, I. Cherniukh, L. Pöttschacher, Y. Shynkarenko, S. Yakunin and M. V. Kovalenko, *Chem. Mater.*, 2019, **31**, 10161–10169.

16 P. F. Fu, Y. L. Sun, Z. G. Xia and Z. W. Xiao, *J. Phys. Chem. Lett.*, 2021, **12**, 7394–7399.

17 Z. W. Xiao, Z. N. Song and Y. F. Yan, *Adv. Mater.*, 2019, **31**, 1803792.

18 K. Dave, M. H. Fang, Z. Bao, H. T. Fu and R. S. Liu, *Chem. – Asian J.*, 2020, **15**, 242–252.

19 Q. Q. Fan, G. V. Biesold-McGee, J. Z. Ma, Q. N. Xu, S. Pan, J. Peng and Z. Q. Lin, *Angew. Chem., Int. Ed.*, 2020, **59**, 1030–1046.

20 G. Q. Ji, C. Z. Han, S. L. Hu, P. F. Fu, X. Chen, J. G. Guo, J. Tang and Z. W. Xiao, *J. Am. Chem. Soc.*, 2021, **143**, 10275–10281.

21 B. B. Su, G. J. Zhou, J. L. Huang, E. H. Song, A. Nag and Z. G. Xia, *Laser Photonics Rev.*, 2020, **15**, 2000334.

22 Q. Zhou, L. Dolgov, A. M. Srivastava, L. Zhou, Z. L. Wang, J. Shi, M. D. Dramićanin, M. G. Brik and M. M. Wu, *J. Mater. Chem. C*, 2018, **6**, 2652–2671.

23 Q. K. Ba, A. Jana, L. H. Wang and K. S. Kim, *Adv. Funct. Mater.*, 2019, **29**, 1904768.

24 H. Y. Ye, Q. Zhou, X. Niu, W. Q. Liao, D. W. Fu, Y. Zhang, Y. M. You, J. Wang, Z. N. Chen and R. G. Xiong, *J. Am. Chem. Soc.*, 2015, **137**, 13148–13154.

25 A. K. Guria, S. K. Dutta, S. Das Adhikari and N. Pradhan, *ACS Energy Lett.*, 2017, **2**, 1014–1021.

26 G. C. Hu, B. Xu, A. F. Wang, Y. Guo, J. J. Wu, F. Muhammad, W. Meng, C. Y. Wang, S. Q. Sui, Y. Liu, Y. C. Li, Y. Zhang,

This journal is © The Royal Society of Chemistry 2022

J. Mater. Chem. C, 2022, **10**, 2095–2102 | **2101**

Y. G. Zhou and Z. T. Deng, *Adv. Funct. Mater.*, 2021, **31**, 2011191.

27 T. M. Jiang, W. B. Ma, H. Zhang, Y. Tian, G. Lin, W. G. Xiao, X. Yu, J. B. Qiu, X. H. Xu, Y. Yang and D. X. Ju, *Adv. Funct. Mater.*, 2021, **31**, 2009973.

28 F. Locardi, M. Cirignano, D. Baranov, Z. Dang, M. Prato, F. Drago, M. Ferretti, V. Pinchetti, M. Fanciulli, S. Brovelli, L. De Trizio and L. Manna, *J. Am. Chem. Soc.*, 2018, **140**, 12989–12995.

29 W. Y. Liu, Q. L. Lin, H. B. Li, K. F. Wu, I. Robel, J. M. Pietryga and V. I. Klimov, *J. Am. Chem. Soc.*, 2016, **138**, 14954–14961.

30 J. D. Majher, M. B. Gray, T. A. Strom and P. M. Woodward, *Chem. Mater.*, 2019, **31**, 1738–1744.

31 A. Biswas, R. Bakthavatsalam and J. Kundu, *Chem. Mater.*, 2017, **29**, 7816–7825.

32 C. K. Zhou, Y. Tian, O. Khabou, M. Worku, Y. Zhou, J. Hurley, H. R. Lin and B. W. Ma, *ACS Appl. Mater. Interfaces*, 2017, **9**, 40446–40451.

33 S. K. Dutta, A. Dutta, S. Das Adhikari and N. Pradhan, *ACS Energy Lett.*, 2018, **4**, 343–351.

34 G. J. Zhou, X. X. Jiang, M. Molokeev, Z. S. Lin, J. Zhao, J. Wang and Z. G. Xia, *Chem. Mater.*, 2019, **31**, 5788–5795.

35 L. K. Gong, Q. Q. Hu, F. Q. Huang, Z. Z. Zhang, N. N. Shen, B. Hu, Y. Song, Z. P. Wang, K. Z. Du and X. Y. Huang, *Chem. Commun.*, 2019, **55**, 7303–7306.

36 C. L. Jiang, N. Zhong, C. H. Luo, H. C. Lin, Y. Y. Zhang, H. Peng and C. G. Duan, *Chem. Commun.*, 2017, **53**, 5954–5957.

37 S. Zhang, Y. F. Zhao, J. D. Zhou, H. Ming, C. H. Wang, X. P. Jing, S. Ye and Q. Y. Zhang, *Chem. Eng. J.*, 2021, **421**, 129886.

38 M. Z. Li, J. Zhou, M. S. Molokeev, X. X. Jiang, Z. S. Lin, J. Zhao and Z. G. Xia, *Inorg. Chem.*, 2019, **58**, 13464–13470.

39 G. J. Zhou, Z. Y. Liu, M. S. Molokeev, Z. W. Xiao, Z. G. Xia and X.-M. Zhang, *J. Mater. Chem. C*, 2021, **9**, 2047–2053.

40 M. Zhao, H. X. Liao, M. S. Molokeev, Y. Y. Zhou, Q. Y. Zhang, Q. L. Liu and Z. G. Xia, *Light Sci. Appl.*, 2019, **8**, 38.

41 L. Y. Lian, P. Zhang, G. Liang, S. Wang, X. Wang, Y. Wang, X. W. Zhang, J. B. Gao, D. L. Zhang, L. Gao, H. S. Song, R. Chen, X. Z. Lan, W. X. Liang, G. D. Niu, J. Tang and J. B. Zhang, *ACS Appl. Mater. Interfaces*, 2021, **13**, 22749–22756.

42 S. Y. Wang, X. X. Han, T. T. Kou, Y. Y. Zhou, Y. Liang, Z. X. Wu, J. L. Huang, T. Chang, C. Y. Peng, Q. L. Wei and B. S. Zou, *J. Mater. Chem. C*, 2021, **9**, 4895–4902.

43 A. Sen, D. Swain, T. N. Guru Row and A. Sundaresan, *J. Mater. Chem. C*, 2019, **7**, 4838–4845.

44 S. J. Clark, M. D. Segall, C. J. Pickard, P. J. Hasnip, M. I. J. Probert, K. Refson and M. C. Payne, *Z. Kristallogr.*, 2005, **220**, 567–570.

45 J. P. Perdew, K. Burke and M. Ernzerhof, *Phys. Rev. Lett.*, 1996, **77**, 3865–3868.

46 G. Sheldrick, *Acta Crystallogr., Sect. A: Found. Crystallogr.*, 2008, **64**, 112–122.

47 Y. F. Zhao, R. R. Yang, W. Wan, X. P. Jing, T. Wen and S. Ye, *Chem. Eng. J.*, 2020, **389**, 124453.

48 H. Y. Huang, R. T. Yang, D. Chinn and C. L. Munson, *Ind. Eng. Chem. Res.*, 2003, **42**, 2427–2433.

49 R. Pang, C. Li, L. Shi and Q. Su, *J. Phys. Chem. Solids*, 2009, **70**, 303–306.

50 S. P. Lee, C. H. Huang, T. S. Chan and T. M. Chen, *ACS Appl. Mater. Interfaces*, 2014, **6**, 7260–7267.

51 X. F. Zhou, W. Y. Geng, J. Y. Li, Y. C. Wang, J. J. Ding and Y. Y. Wang, *Adv. Opt. Mater.*, 2020, **8**, 1902003.

52 H. Siddique, Z. L. Xu, X. D. Li, S. Saeed, W. T. Liang, X. Q. Wang, C. Gao, R. C. Dai, Z. P. Wang and Z. M. Zhang, *J. Phys. Chem. Lett.*, 2020, **11**, 9572–9578.

53 J. Ruiz-Fuertes, S. López-Moreno, J. López-Solano, D. Errandonea, A. Segura, R. Lacomba-Perales, A. Muñoz, S. Radescu, P. Rodríguez-Hernández, M. Gospodinov, L. L. Nagornaya and C. Y. Tu, *Phys. Rev. B: Condens. Matter Mater. Phys.*, 2012, **86**, 125202.

54 Z. H. Leng, R. F. Li, L. P. Li, D. K. Xue, D. Zhang, G. S. Li, X. Y. Chen and Y. Zhang, *ACS Appl. Mater. Interfaces*, 2018, **10**, 33322–33334.

55 K. A. Denault, J. Brgoch, M. W. Gaultois, A. Mikhailovsky, R. Petry, H. Winkler, S. P. DenBaars and R. Seshadri, *Chem. Mater.*, 2014, **26**, 2275–2282.

56 Z. Q. Ming, J. W. Qiao, M. S. Molokeev, J. Zhao, H. C. Swart and Z. G. Xia, *Inorg. Chem.*, 2020, **59**, 1405–1413.

57 L. Zhou, J. F. Liao, Z. G. Huang, J. H. Wei, X. D. Wang, H. Y. Chen and D. B. Kuang, *Angew. Chem., Int. Ed.*, 2019, **58**, 15435–15440.

58 W. Baur, *Acta Crystallogr., Sect. B: Struct. Crystallogr. Cryst. Chem.*, 1974, **30**, 1195–1215.

2102 | *J. Mater. Chem. C*, 2022, **10**, 2095–2102

This journal is © The Royal Society of Chemistry 2022